Received: 8 August 2022 | Revised: 12 September 2022 | Accepted: 23 September 2022

DOI: 10.1002/jbio.202200252

RESEARCH ARTICLE

JOURNAL OF BIOPHOTONICS

Reflective FT-NIR and SERS studies of HER-II breast cancer biomarker using plasmonic-active nanostructured thin film immobilized oriented antibody

Mohammad E. Khosroshahi[1,2] | **Yesha Patel**[1,3]

[1]Nanobiophotonics and Biomedical Research Laboratory, M.I.S. Electronics Inc., Richmond Hill, Ontario, Canada

[2]Institute for Advanced Non-Destructive & Diagnostic Technologies (IANDIT), University of Toronto, Toronto, Ontario, Canada

[3]Department of Biochemistry, University of Waterloo, Waterloo, Ontario, Canada

Correspondence
Mohammad E. Khosroshahi, Nanobiophotonics and Biomedical Research Laboratory, M.I.S. Electronics Inc., Richmond Hill, ON L4B 1B4, Canada.
Email: khosrom@mie.utoronto.ca; m.khosro@miselectronics.com

Abstract

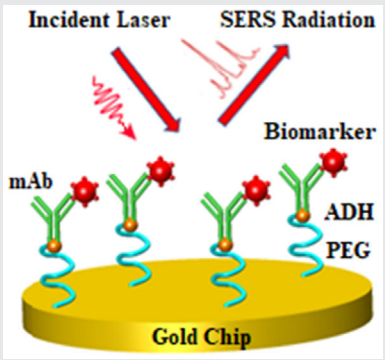

We describe the fabrication of plasmonic-active nanostructured thin film substrate as a label-free surface-enhanced Raman scattering (SERS)-based biosensor immobilized covalently with monoclonal HER-II antibody (mAb) to detect overexpressed HER-II as a biomarker in breast cancer serum (BCS). Oriented conjugation of mAb via hydrazone linkage to provide higher mAb accessibility was characterized by UV-vis and reflective Fourier transform near-infrared (FT-NIR) spectroscopic techniques. The interaction of BCS with mAb was studied by FT-NIR and nonresonant SERS at 637 nm. The results showed detection of glycoprotein content at different laser powers including a rise in amino acid and glycan content with varying results at higher power. With nonresonant SERS we observed nonlinear behavior of peak intensity. Analysis of variance was implemented to determine the effect of laser power which was found not to be a contributing factor. However, at the nanoscale, factors including the heating effect and aggregation of molecules can contribute to the nonlinearity of peak intensity.

KEYWORDS

AFM, biomarker, blood serum, oriented antibody, reflective FT-NIR, SERS, thin film

1 | INTRODUCTION

Cancer is a major public health problem that causes a high rate of morbidity and mortality worldwide. Breast cancer (BC) is the second leading cause of mortality worldwide next to lung cancer, with it being more severe in developing countries [1, 2]. Thus, to reduce the significant disability, suffering and deaths caused by cancer, effective and affordable programs in early diagnosis, screening, treatment and palliative care are needed.

The main drawbacks of mammography include the use of X-rays, pain and discomfort during the screening process, risk of false positive and negative responses, undetectability of lesions less than 0.5 cm in size, negative psychological effects resulting from false-positive results, limited sensitivity for the detection of dense breast tissues, radiation side effects and unselective and unnecessary exposure of the healthy tissues [3, 4]. Other well-established molecular bioimaging systems that aid the diagnosis of tumor techniques are magnetic resonance

imaging (MRI), positron emission tomography (PET), single-photon emission computed tomography (SPECT), computerized tomography (CT) and ultrasound (US). Despite their advantages, they bear some serious limitations including injection of gadolinium, inability to be used for patients with a pacemaker or breast reconstruction, requirement of radio-nucleotide facilities, use of iodine-based compounds, expensive equipment, low sensitivity, low spatial resolution and risks of positive and negative false responses.

Blood-based biomarkers have great potential in noninvasive cancer screening and reducing the total national economic burden. A biomarker has a broad definition; it is a biochemical substance that consists of either the tumor itself or the host in reaction to the tumor's presence that indicates malignant tissues from benign and is measurable in tissues or body fluids such as blood and urine [5]. By analyzing the biomarkers, diagnostic tests may be able to provide information about early tumor development to detect a cancer such as BC at an early and more treatable stage. However, they should be noninvasive, easily measured, inexpensive and produce rapid and reliable results. Noninvasive techniques such as in vitro diagnostics have a number of advantages: (a) no direct interaction with the human body, making it accessible without invasive surgeries and suffering, (b) provide a rapid and accurate assessment of tissues or biofluids, regarding disease diagnosis and therapy, (c) tests are performed on samples instead of human body, increasing the safety by avoiding the possible infection via contact, (d) rapidly provide valuable information on a patient's healthcare conditions and (e) enable early diagnosis, which makes treatment of disease relatively easier and more comfortable. In recent years, noninvasive techniques have been used to determine the biomarker levels in electrochemical immunosensors [6–8], electrochemiluminescence immunosensors [9], lectin-based optical sensing [10], quartz crystal microbalances [11], silicon-based ultrasonic immunoassays [12] and optofluidic ring resonator sensors [13].

The overexpression of the HER-II receptor transmembrane glycoprotein by tumor cells has gained significant attention as a biomarker as well as a target for therapeutic treatments as they are essential in controlling cell growth and differentiation [14]. The receptor has a 630 amino acid extracellular domain that is proteolytically cleaved which allows for its shedding from the tumor cell surface and the detection of the domain in patient blood serum [15]. Nearly half of all human proteins are glycosylated, and these carbohydrate glycans are of use when it comes to cancer biomarker detection in biosensor applications [16]. The extracellular domain of HER-II has seven potential N-linked glycosylation sites that can be used for the detection of carbohydrate presence along with the detection of specific protein signals from the biomarker itself [15]. N-linked glycans have specific roles in protein folding, cell-cell recognition, adhesion and signaling, all of which are important in cancer metastasis. With regards to BC, high mannose, fucosylated and complex glycans are the most relevant N-linked glycans [17]. Using Raman spectroscopy (RS), the position and intensity of the bands in their respective spectra can be used to detect HER-II biomarker binding to a sensor surface based on carbohydrate and protein content.

Raman scattering is an inelastic scattering of photons, which is a result of the interaction between the incident light and a molecule excites a molecular vibration. Thus, the Raman signals are represented by a frequency shift measured in wavenumber (cm^{-1}) and are characteristic of the particular molecular species, with signal intensity proportional to the number of scattering molecules in the path of the light [18]. As such, these Raman shifts can aid in cancer diagnostics by identifying biochemical differences between normal and tumor tissues due to an increase in the concentration of proteins, lipids and nucleic acids in tumors [19–21]. However, the weak intensity of Raman signal can be enhanced 10^5 to 10^{14} times by adsorption of sample molecules onto metal surface via surface-enhanced Raman scattering (SERS) spectroscopy. There are two types of surface plasmons (SPs). First, propagating where the frequency of the incident light and the oscillating SP are very close or equal and light waves can couple, excite and propagate the SPs at the metal-dielectric interface called surface plasmon polaritons (SPP) generated on noble metallic thin films such as Au or Ag. These are the collective charge-density waves, and the metal exhibits field enhancement at the surface [22]. Second, non-propagating SPs are called localized surface plasmon resonance (LSPR), which are generated on the surface of plasmonic nanoparticles (PNP). The main mechanisms of SERS are thought to be due to: (a) electromagnetic enhancement where the intensity of the incident light is caused by LSPR and referred to as *hot spots*. An induced dipole due to the plasmon oscillation enhances the local electric field at the surface of the PNP, and thus, strong light absorption and scattering occur at the SPR frequency [23]. For scattering to occur, the surface must be roughened to produce a perpendicular component to the plasma. Thus, the plasmon energy causes the RS to occur in the analyte molecule. The energy is transferred back to the plasmon, and the radiation is shifted in frequency due to the energy difference between oscillation of light and molecular vibration, and (b) is the chemical enhancement or charge transfer mechanism where the complexation of the target analyte to the PNP results in charge transfer

between the adsorbed molecule and the metal surface in either direction [24]. SERS is a nondestructive, specific and highly powerful technique, which extensively has been utilized for biosensing and the detection of chemical and biological analyte molecules at very low concentrations [25–30].

SERS active substrates can be colloidal, that is, solution-based, solid-supported substrates where various types, shapes and sizes of nanostructures including spherical nanoparticles, nanorods, nanostars, nanoshells and thin film substrate where a controlled layer of plasmonic material is vapor deposited on the substrate by different techniques such as electron beam [31, 32]. In particular, thin films have been a topic of research in both nanotechnology and biochemical applications, with uses in various electrochemical and optical sensors for signal enhancement [33–35]. Gold metal surfaces are photostable and biocompatible because of their inert surface, nontoxic, involve relatively easy synthesis, allow for functionalization and surface conjugation chemistry, there is an absence of photobleaching and they are resistant to oxidation [36, 37]. In fact, the surface has a high affinity for thiol (—SH) groups, enabling them to be PEGylated, that is, functionalized with thiol-PEG via strong Au—S bonds, which for in vivo applications, reduces the uptake of AuNS by the liver and spleen and prolongs the half-life in blood [38].

Even in the ideal case of perfectly smooth metal surfaces, there is the likelihood of intensive SP scattering on possible surface imperfections and defects on the nanometer scale (eg, metal grains) which can contribute to plasmon confinement and related field enhancement effects [39]. The planar nanometer-thin film is 2D nanomaterial itself and is plasmonic-active, but it is not considered a plasmonic-active nanostructured thin film (PANTF) as in our case. The PANTFs are unique kinds of nanostructures with the properties of both thin films and individual nanoparticles, see Figure 2E. Monoclonal antibodies (mAb) are increasingly developed and utilized in anticancer detection and therapies [40, 41]. Here, an anti-HER-II mAb is used to target the HER-II biomarker in breast cancer serum (BCS). Therefore, the conjugation of a suitable mAb to gold film or AuNS can be used for high-performance SERS probes as a nondestructive alternative technology for rapid and selective ultrasensitive biomolecular detection such as biomarkers, either cellular or humoral, as well as compositional analysis [26, 42]. SERS-based immunoassays are especially valuable for the detection of low abundance biomarkers.

The near-IR region contains overtone and combination bands of fundamental vibrational modes, namely functional groups containing a relatively heavy atom (C, N, O and S) attached to a hydrogen atom [43]. Thus, Fourier transform near-infrared spectroscopy (FT-NIR), as a nondestructive chemical analysis technology, can analyze various materials and provide rich information on molecular structures. As such, FT-NIR has emerged a reliable method of biochemical fingerprinting and is particularly useful in analyzing surface chemistries in biosensor synthesis and fabrication methods [44]. Working at the nanoscale allows for more accurate NIR investigations as it involves using small biomolecules which are optimal for NIR spectroscopy [45]. In this study, FT-NIR is used as a technique to investigate the surface chemistry during sensor fabrication as well as for the detection of biomarker binding.

One aspect of novelty of the present work is the oriented conjugation of the mAb on the PEGylated surface of the gold chip via an adipic dihydrazide (ADH) linkage. This enables high selectivity and makes the antigen-binding regions more accessible unlike traditional nonselective amide linkages that result in the hindrance of the binding sites [46, 47]. The orientation of the analyte on the surface is important since the scattering originates from the component of the plasmon perpendicular to the surface and this, in turn, is related to the molecular polarization vertical to the surface. Thus, at low concentrations, proteins on the gold surface tend to lie within the aromatic amino acid ring plane parallel to the surface but as monolayer coverage of the surface is approached, the rings tend to stack with the plane perpendicular to the surface [48]. The selective orientation of the mAb on the gold surface is accomplished by activating the glycosylated oligosaccharide moieties in the constant (Fc) region of the mAb with sodium periodate. Once activated, the Fc regions can form highly stable hydrazone bonds with ADH molecules, effectively allowing the targeted orientation of the antibodies and leaving the antigen-binding sites free for binding. Contrastingly, traditional carbodiimide chemistry methods of forming antibody bioconjugates rely on amide bonds that are not targeted to the Fc region. The primary amine (—NH_2) groups involved in such EDC/sulfo-NHS chemistry methods are found in all regions of the antibody, so the mAb can be bound to a carboxyl-functionalized (—COOH) surface in any orientation. In particular, the antigen-binding regions (ie, variable Fab region) also contain primary amine groups which make those regions susceptible to amide bond formation, thus rendering them unavailable for antigen binding [49, 50]. Therefore, the efficiency of the biomarker detection is correspondingly improved with the EDC/ADH hydrazone bond chemistry method due to the selective bond formation at the Fc region, allowing for improved availability of the Fab region that mediates antigen binding. The purpose of this research is to: (a) immobilize and characterize an

oriented mAb-conjugated thin film gold chip biosensor using UV-vis and FT-NIR spectroscopy, and (b) detect HER-II as a BC biomarker in patient blood serum as well as analyze the composition using a nonresonant 637 nm laser using SERS and FT-NIR spectroscopy.

2 | MATERIALS AND METHODS

2.1 | Oriented functionalization of gold chip

Inside a biosafety cabinet (Class II A2, Labgard, USA), 1 mL of ultrapure water (Invitrogen) was added to a clean 1.5 mL microcentrifuge tube (Biolynx, Canada). Then, 25 mg of a 5K thiol-PEG-carboxyl linker molecule (SH-PEG-COOH, Biochempeg, USA) was weighed on the analytical balance (Sartorius, USA) and added to the tube containing the water. The tube was mixed by vortexing at 2200 rpm (RK-04729-07, Cole-Parmer, Canada) for 30 seconds to ensure the PEG dissolved.

Commercially available sealed gold chips (SPR-1000-050: SPRchip, Biolynx, Canada) were prepared by conventional e-beam evaporation technique (Platypus Technologies). For the PEG-ylation reaction, 800 μL of the PEG linker solution was added to the empty chip container. Then, the chip was placed in the container with the active surface facing down in direct contact with the linker solution. The cap was lightly sealed, and the container was left on the orbital shaker (RK-51700-13, Cole-Parmer, Canada) overnight at room temperature at 150 rpm. The container was covered with a beaker to minimize any evaporation.

First, the PEGylated chip was rinsed with water and then with 70% ethanol (Fisher, BP82031GAL) to remove the excess PEG linker molecules. The chip was air-dried and characterized with reflectance FT-NIR. Once the gold-PEG chip had been characterized, a 5 mm × 5 mm active area was marked on the chip. This was done by taping the chip so that only a 5 mm × 5 mm square was exposed in the center; the rest of the chip was covered with tape. The active area was designated to concentrate the chemicals and mAb in a smaller area of the chip instead of functionalizing the whole surface. On the analytical balance, 32 mg of adipic acid di-hydrazide (ADH, Sigma-Aldrich, Canada), and 16 mg of N-(3-dimethylaminopropyl)-N′-ethyl-carbodiimide hydrochloride (EDC, Sigma-Aldrich, Canada) were measured. Both powders were added to a tube containing 1.1 mL of ultrapure water to be dissolved. From this tube, 800 μL of the solution was added to the empty chip container. The gold surface of the chip was placed face-down in the container. The cap was lightly sealed, and the container was left on the orbital shaker for 3 hours at room temperature at 150 rpm. The container was covered with a beaker to minimize any evaporation. Once the time was complete, the gold surface was rinsed with ultrapure water to remove excess reagents. The chip was once again characterized by FT-NIR.

2.2 | Oriented conjugation of gold chip

The bottle of ultrapure water was opened inside the biosafety cabinet, and 1 mL of water was transferred to a clean 1.5 mL microcentrifuge tube. Then, 14.19 mg of sodium phosphate (Na_2HPO_4–, MW = 141.96 g/mol, Sigma Aldrich) was weighed using the analytical balance. The sodium phosphate was added to the tube containing 1 mL of water to make a 100 mM buffer. The anti-HER-II antibody (Ab, MAB1129, R&D Systems, Canada) was thawed overnight in a fridge (4°C). The mAb had a dry weight of 100 μg, and was reconstituted to a concentration of 0.5 mg/mL as recommended by the manufacturer. The reconstitution was done by adding 200 μL of PBS to the dry weight mAb. The mAb was then divided into four tubes (each containing 25 μg of antibody in 50 μL PBS) and stored at −20°C. To complete the buffer exchange, the phosphate-buffered saline (PBS, pH 7.4, Gibco, USA) of the mAb was to be exchanged with the newly prepared 100 mM sodium phosphate buffer. To do this, two 30 kDa centrifugal filter devices (UFC503096, Millipore Sigma) were used. One filter unit (ie, spin column) was used for the mAb sample, and one was used as a balance for the microcentrifuge. The filter was placed in an empty labeled microcentrifuge tube, and then the entire mAb volume (50 μL) was transferred to the filter unit. The spin columns were balanced and centrifuged at 14,000 rpm for 10 minutes. The microcentrifuge tube (now containing PBS) was discarded and the mAb remained on the filter unit. Then, 25 μL of 100 mM sodium phosphate buffer was added to a new microcentrifuge tube as the recovery buffer. The filter unit containing the mAb was placed upside down in the tube containing recovery buffer for the reverse spin. The tubes were balanced and centrifuged at 3000 rpm for 2 minutes to recover the mAb from the filter unit. Once completed, the filter units were discarded. The microcentrifuge tube now contained 25 μL of mAb at a concentration of 1 mg/mL.

For the mAb activation and purification, a new "coupling" buffer was prepared, consisting of 10 mM sodium phosphate, 0.15 M sodium chloride at pH 7.5. To prepare 10 mL of the buffer, 8 mL of distilled water was added to a glass beaker. Then, 14.02 mg of sodium phosphate and 87.68 mg of sodium chloride (NaCl, MW = 58.44 g/mol, Sigma Aldrich) were measured and added to 8 mL of

water. A pH meter (BLU2300E, Combo Bluelab, New Zealand) was used to measure the initial pH, which was 8.6. To lower the pH to 7.5, diluted hydrochloric acid needed to be added. The diluted hydrochloric acid was prepared by adding 5 μL of 37% hydrochloric acid (HCl, Sigma Aldrich) to 4 mL of distilled water. The pH of the buffer was adjusted by adding 1.6 mL of dilute HCl to the beaker. Once the pH reached 7.5, water was added until the final volume reached 10 mL. Once the buffer exchange was completed, the mAb needed to be activated to react with the hydrazide. The mAb was activated with sodium periodate ($NaIO_4$, MW = 213.89 g/mol, Sigma Aldrich). A 0.1 M $NaIO_4$ solution was prepared by adding 2.14 mg of $NaIO_4$ to 100 μL ultrapure water in a clean 1.5 mL microcentrifuge tube. The $NaIO_4$ tube was mixed and wrapped in aluminum foil to protect it from light. Then, 5 μL of the prepared 0.1 M $NaIO_4$ solution was added to the tube containing 25 μL of Ab. The tube was vortexed at 2200 rpm for 30 seconds and then incubated at room temperature for 45 minutes at 275 rpm on the orbital shaker. After incubation, the reaction was quenched by adding 200 μL of PBS to the tube of mAb. At this point, the existing mAb buffer was exchanged to the new coupling buffer prepared in the previous step using the spin columns. The same steps as in the previous buffer exchange were followed using the entire volume of mAb (~230 μL). The final recovery buffer used for the reverse spin was 50 μL of coupling buffer. The final mAb volume was now 50 μL at a concentration of 0.5 mg/mL.

The functionalized gold chip was placed in its container, with the gold surface facing up. At this point, 100 μL of the coupling buffer was added to the tube containing 50 μL of mAb. The total volume of 150 μL was transferred to the surface of the functionalized gold chip to submerge the active area. The cap was lightly sealed, and the container was left on the orbital shaker overnight at room temperature at 150 rpm. The container was covered with a beaker to minimize any evaporation. To prevent the hydrazone bond (ie, the bond between ADH-mAb) from reversing, the reaction had to be stabilized by the addition of 2 μL of 1 M ethanolamine ($NH_2CH_2CH_2OH$, MW = 61.09 g/mol, Sigma Aldrich). The ethanolamine was already supplied at a 1 M concentration. It was handled in the fume hood (ISOLA, Mystaire, USA). Once the ethanolamine had been added to the surface of the chip (which had been incubating overnight), the functionalized chip was sealed and incubated at room temperature at 150 rpm on the orbital shaker for 1 hour with a beaker over top to prevent evaporation. To block the surface of the chip which did not bind any mAb, a 10% (w/v) BSA solution was prepared by adding 1.5 mg of BSA to 15 μL of coupling buffer in a clean microcentrifuge tube. Then, the whole volume of the BSA was added to the surface of the sample gold chip (ie, Gold-PEG-ADH-mAb). The chip was then incubated at room temperature for 10 minutes at 150 rpm on the orbital shaker. The chip was sealed in its container and covered with a beaker. The excess BSA and reagents were rinsed off with PBS. After air-drying, the Gold-PEG-ADH-mAb was characterized with FT-NIR and RS.

2.3 | Interaction of Gold-PEG-ADH-Ab and HER-II

In the biosafety cabinet, the BCS (#2372644, Precision Biospecimen, USA) overexpressed with HER-II was diluted in a prepared 0.01 M PBS buffer (adjusted to pH 6.0 with HCl) in a clean 1.5 mL microcentrifuge tube (4 μL BCS:56 μL PBS buffer). To this dilution, 100 μL of 2-(N-morpholino) ethanesulfonic acid (MES) (Sigma Aldrich-M8250-25G, pH 6.0) was added to make the total volume of serum dilution 160 μL. The BCS dilution was then vortexed at 2200 rpm for 30 seconds. The entire volume of prepared serum dilution was added to the surface of the functionalized gold chip while the chip was inside its original container to submerge the active area. The cap was sealed and incubated at room temperature at 150 rpm on the orbital shaker for 1 hour with a beaker over top to prevent evaporation. After incubation, the excess reagents and unbound serum proteins were rinsed off with the same MES buffer. The chip was air-dried before characterization with FT-NIR and RS.

2.4 | Characterization methods

Prior to surface functionalization, the absorbance of the ligands was measured at each stage by UV-vis spectrometer (Jenway 7205-Cole-Parmer-Canada) with a 198 to 800 nm spectral range. The experimental setup for the reflectance FT-NIR setup is shown in Figure 1A. The gold chip was characterized at different stages using FT-NIR Nano Quest spectrometer (NanoQuest 2.5, Ocean Insight) to obtain reflectance spectra. The parameters were set to 5 seconds integration time and 8 nm resolution. A 200 μm bifurcated reflectance probe (RP28, Thorlabs, USA) was used connected to the tungsten halogen light source (HL-2000-HP, Ocean Insight). The probe was positioned 10 mm perpendicular to the surface of the chip, and the background reading was a solid white foam surface. The experimental setup for the RS setup is shown in Figure 1B. The chip was characterized using RS after conjugation and interaction with BCS using the 638 nm Raman probe (RIP-RPB-638-FC-APC-SMA, Ocean Insight, USA) in a perpendicular direction to the surface of the chip at a distance

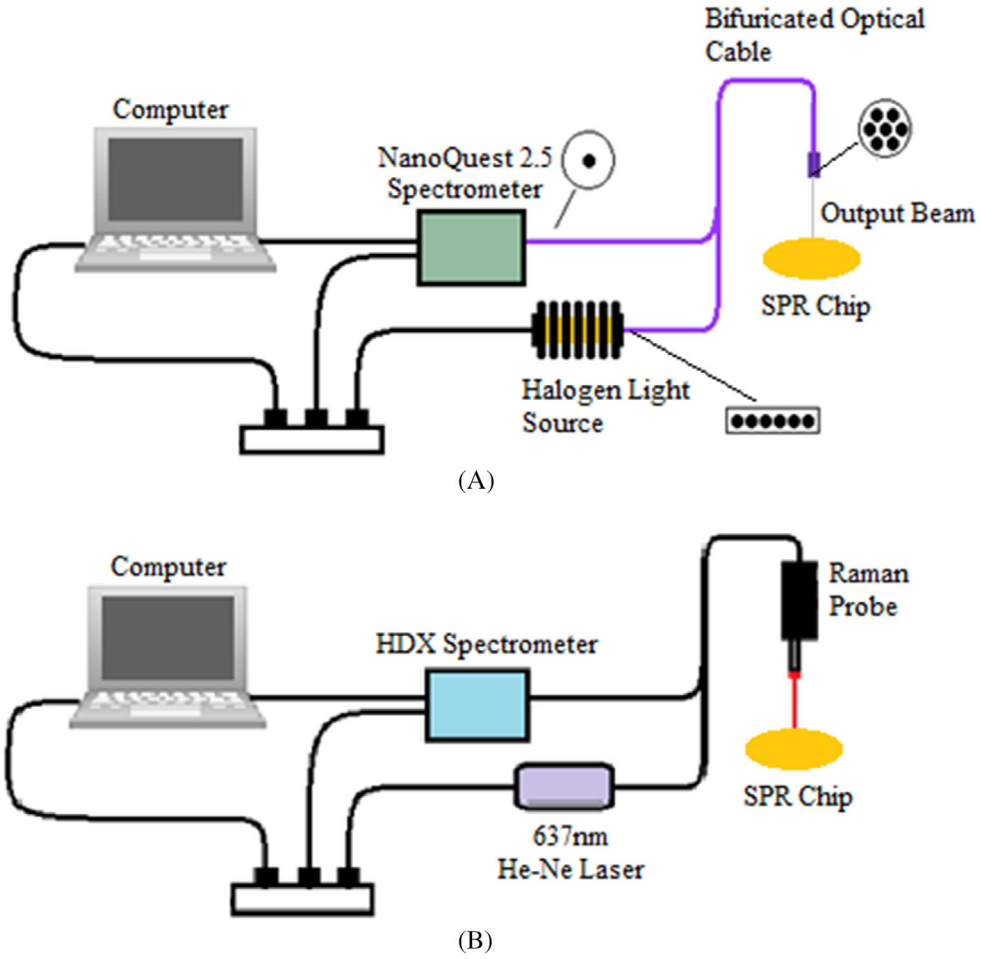

FIGURE 1 Experimental setups for characterization methods of the functionalized gold chip biosensor surface using (A) reflectance FT-NIR and (B) Raman (SERS) spectroscopy. FT-NIR, Fourier transform near-infrared; SERS, surface-enhanced Raman scattering

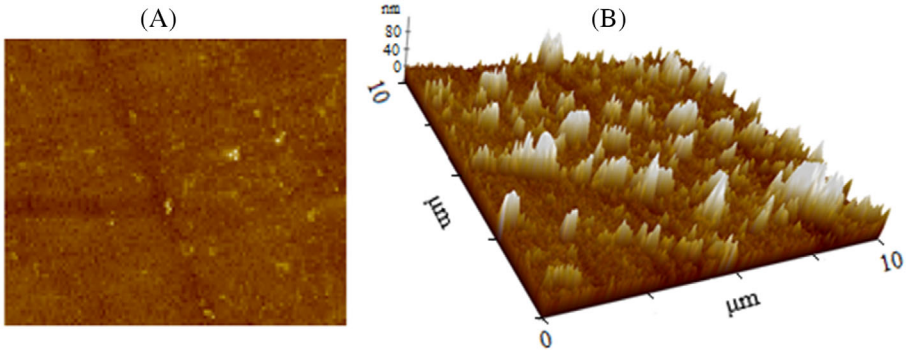

FIGURE 2 Noncontact AFM characterization of untreated gold thin film surface at 10 μm resolution using (A) 2D and (B) 3D modes

of 7.5 mm (ie, the focal distance of the probe). The probe was connected to the 637 nm laser (S1FC637, Thorlabs, USA) and an Ocean HDX spectrometer (OCEAN-HDX-VIS-NIR, Ocean Insight, USA). In the Oceanview software, the parameters were set to 5 seconds integration time, 3 scan average, and 5 boxcar width. The nonlinearity correction was applied, and the clean peaks option was selected. A dark background with the 637 nm laser off was taken. The experiment was performed at 2 mW, 4 mW, and 8 mW to observe the effect of power on the results.

To visualize the surface quality of the untreated gold chip, 2D (Figure 2A) and 3D (Figure 2B) topographic images were recorded in noncontact atomic force microscopy (AFM) mode (Park NX10, USA). The surface was cleaned with ethanol prior to AFM characterization. The thickness of the thin film was determined to be ≈ 4 nm using AFM. The images show various surface protrusions which are likely a result of the e-beam gold deposition process, and thus can contribute to a roughened surface and consequent optical signal enhancements [51, 52].

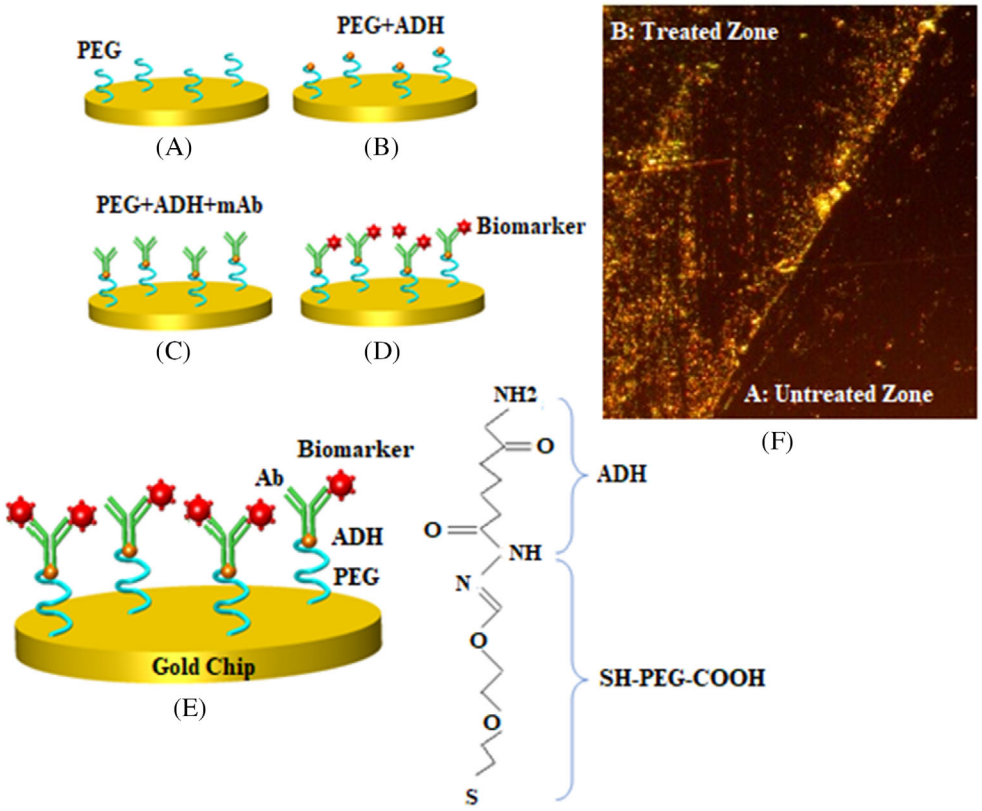

FIGURE 3 (A) Functionalization of gold chip surface with SH-PEG-COOH linker molecule; (B) conjugation of ADH molecule to PEG linker via EDC/ADH chemistry; (C) selective formation of stable hydrazone bond between periodate-activated anti-HER-II mAb at the fc region and the ADH molecule; (D) HER-II biomarker binding to gold chip surface at the available antigen-binding sites; (E) chemical structure of oriented antibody linkage with respect to the gold surface; (F) microscope image of the gold surface showing treated and untreated regions of the sensor. ADH, adipic dihydrazide

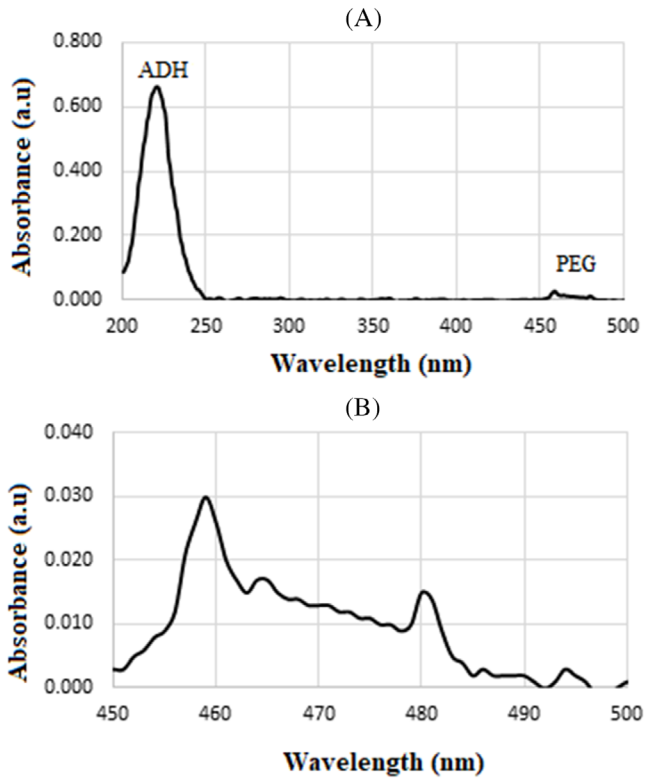

FIGURE 4 UV-vis absorbance of (A) colloidal gold nanourchins (100 nm) functionalized with SH-PEG-COOH-ADH using the same method as the gold chip functionalization and (B) magnification of the PEG absorbance between 450 and 500 nm

3 | RESULTS AND DISCUSSION

To prepare the bio-conjugated gold chip with a selective antibody orientation, a number of steps were taken as schematically outlined in Figure 3. First, the surface of the chip was PEGylated with an SH-PEG-COOH linker molecule as seen in Figure 3A. The —COOH group at the end of the PEG linker is essential in the EDC/ADH reaction to prepare the chip surface for mAb binding. Next, the synthesis of the PEG-ADH bond was carried out via derivation of the PEG-COOH linker with EDC/ADH chemistry (Figure 3B). The mAb was activated using sodium periodate oxidation to prepare the Fc regions for the formation of the hydrazone bond as seen in Figure 3C. The interaction process with the BCS biomarker (HER-II) is illustrated in Figure 3D, with a magnified version of the labeled components and corresponding chemical structure in Figure 3E. A microscope image (Microscope net, OMAX-18MP) of the chip showing the untreated (A) and functionalized (B) zones respectively is shown in Figure 3F.

3.1 | UV-vis spectroscopy

The UV-vis spectra of the surface-functionalized colloidal 100 nm gold nanourchins are shown in Figure 3.

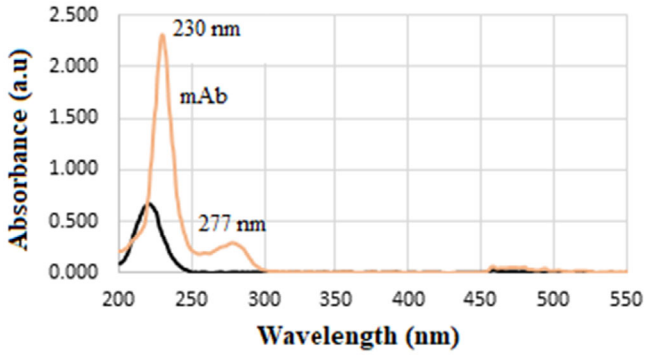

FIGURE 5 UV-vis absorbance of colloidal gold nanourchins (100 nm) functionalized with SH-PEG-COOH-ADH following conjugation with anti-HER-II mAb via hydrazone bond formation

Figure 4A shows that the ADH is conjugated to PEG linker with a strong ADH absorbance intensity at ≈220 nm and a weak peak at ≈460 nm, which corresponds to the PEG [53, 54]. Figure 3B is a magnification of the PEG spectrum with a broad band between 455 and 485 nm. This is because PEGs are composed of polyether compounds repeating ethylene glycol units according to the constituent monomer or parent molecule such as ethylene glycol, ethylene oxide or oxyethylene each with the corresponding spectral response [55].

The absorbance spectrum of mAb-conjugated ADH is shown in Figure 5 where the strong peak at 230 nm and a smaller one at 277 nm correspond to tyrosine (Tyr) peaks, which has two standard peaks at about 227 nm and the other between 270 and 290 nm, respectively [56]. Typically, aromatic amino acid side chains exhibit absorption between 240 and 300 nm with a maximum peak at 280 nm. It is noteworthy that the absorption peak of ADH after conjugation of mAb is red-shifted by 2 nm, indicating the increase in size of the chemical structure.

3.2 | FT-NIR spectroscopy

The FT-NIR spectra collected after each functionalized step were used as a means to analyze the chemical bonds and confirm the expected groups were present. As outlined in [57], according to the superposition principle, the noise-free model function of the protein FTIR spectrum $\gamma(\bar{\nu}, T)$ measured at wavenumber $\bar{\nu}$ and temperature T is given by

$$\gamma(\bar{\nu}, T) = \sum_{k=1}^{N} c_k(T)\varepsilon_k(\bar{\nu}), \quad (1)$$

where the sum extends over N absorption bands, with index k which is assumed to be independent of temperature. The shape of the absorption band k is given by $\varepsilon_k(\bar{\nu})$, where k is characteristic for a particular secondary-structure class or amino acid side chain. The amplitude of k is $c_k(T)$, which may be dependent on temperature. The relations between these parameters allow for the analysis of the FT-NIR peaks with focus on peak position as well as the significance of the peak amplitude. Table 1 outlines common peak assignments with FT-NIR spectroscopy [58–61]. A comparison of the reflectance FT-NIR spectra of the unfunctionalized and PEGylated gold chip is shown in Figure 6. By comparing these two spectra, the effects of the functionalization of the surface can be seen by the shift and appearance of new peaks which indicate changes in the surface chemistry. Initially, with the gold chip alone, there are strong signals in the 2100 to 2200 nm region. Contrastingly, after the PEGylation of the gold surface, there is a reduction of the signal

TABLE 1 FT-NIR bands used for tentative assignment at each step of the gold chip biosensor synthesis

Reference's band assignment	Wavelength (nm)
CH_2 combination 1st overtone	1375–1440
O—H 1st stretch overtone	1400–1500
O—H 1st stretch overtone	1429–1667
RNH_2 1st overtone	1485–1515
Aromatic CH 1st overtone	1610–1650
β-sheet	1688–1691, 2055
α-helix	1738
RCO_2H 1st overtone (O—H stretching)	1875–1905
O—H 1st stretch overtone	1875–1915
C═O stretch 2nd overtone	1942
C—H combination	2200–2450

Abbreviation: FT-NIR, Fourier transform near-infrared.

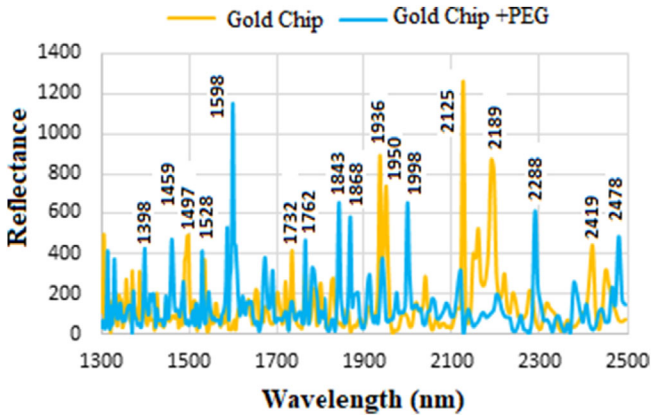

FIGURE 6 Reflectance FT-NIR spectra of gold surface alone and gold surface functionalized with PEG linker molecule (ie, SH-PEG-COOH). FT-NIR, Fourier transform near-infrared

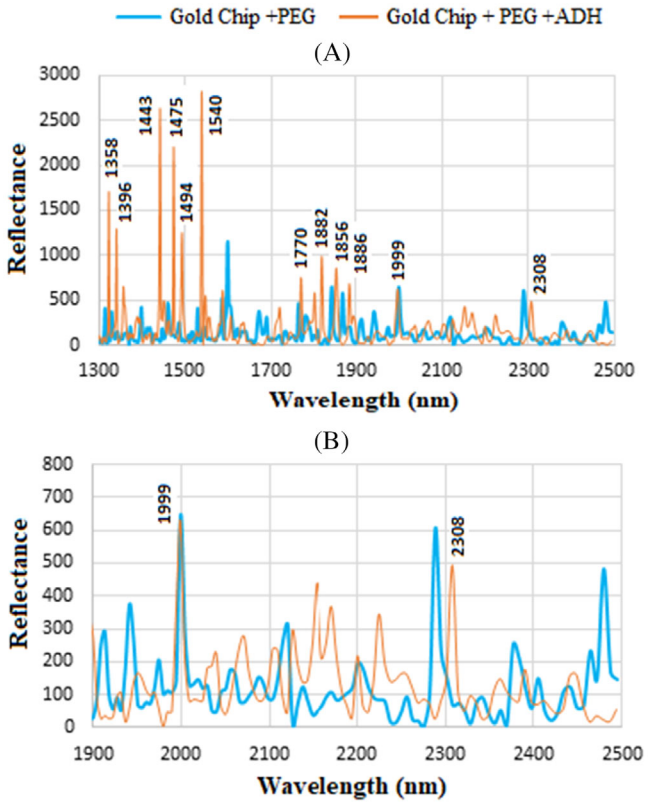

FIGURE 7 (A) Reflectance FT-NIR spectra of gold surface before and after addition of –ADH to the PEG linker via EDC/ADH chemistry in preparation for mAb conjugation. (B) Magnification of 1900 to 2500 nm region. FT-NIR, Fourier transform near-infrared. ADH, adipic dihydrazide; FT-NIR, Fourier transform near-infrared

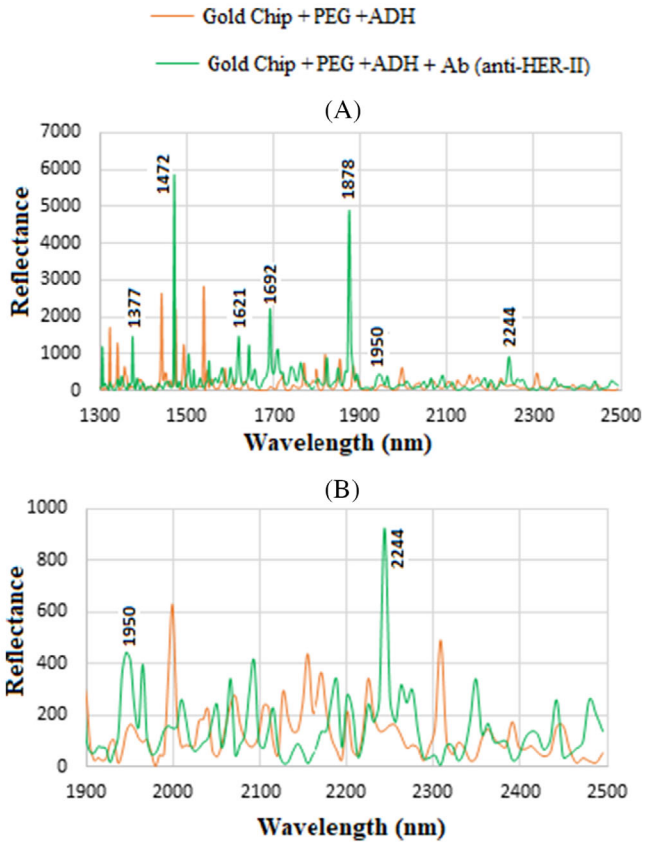

FIGURE 8 (A) Reflectance FT-NIR spectra of gold surface before and after conjugation of anti-HER-II mAb to the gold surface via the formation of a hydrazone bond. (B) Magnification of 1900 to 2500 nm region. FT-NIR, Fourier transform near-infrared

between 2100 and 2200 nm and a new strong signal at 1598 nm, which falls in the O—H 1st stretch overtone region. The O—H bond in the carboxyl group of the PEG linker is responsible for the observed signal, and there is also some activity in the 1800 to 2000 nm region which can be accredited to the C═O stretch 2nd overtone as part of the same carboxyl group. At 2288 nm, there is another new signal which falls in the C—H combination region as part of the organic bonds in the PEG linker. These changes in signal confirm the successful PEGylation of the gold surface.

In preparation for the mAb conjugation, the PEGylated surface was functionalized with ADH (ie, synthesis of PEG-ADH) via the derivation of the —COOH end of the linker using EDC as a facilitator. A comparison of the two spectra is pictured in Figure 6, which shows the changes in signal after the ADH molecule is detected by reflectance FT-NIR. There is an abundance of new signals in the 1300 to 1550 nm region which correspond to the C—H combination and CH_2 combination 1st overtone regions as seen in Figure 7A. This is likely due to the presence of those bonds in the ADH molecule itself. The —NH_2 group in the ADH molecule also contributes to the signals found between 1485 and 1515 nm, as this is the R—NH_2 1st overtone region. The peaks at 1999 nm and 2038 nm as magnified in Figure 7B remain relatively constant, which can be attributed to either the gold chip itself or the C-H combination regions of the PEG molecule, both of which are probable.

The anti-HER-II mAb was activated using sodium periodate and conjugated to the chip via hydrazone bond formation with the ADH molecules. The use of this method allows for selective orientation of the mAb to be anchored at the Fc region, leaving the Fab regions more accessible for antigen-binding. Figure 8A shows a comparison of the FT-NIR spectra of the gold chip before and after mAb conjugation. There are strong signals observed at 1472 and 1878 nm, which likely correspond to an increased number of bonds in the O—H stretch 1st overtone region. There are also new signals between 1600 and 1750 nm which span the α-helix, β-sheet and aromatic CH 1st overtone regions. The aromatic signal likely arises from the presence of aromatic amino acids in the mAb such as phenylalanine (Phe), Tyr, tryptophan (Trp) and histidine (His) [62]. There is a new signal at 2244 nm as

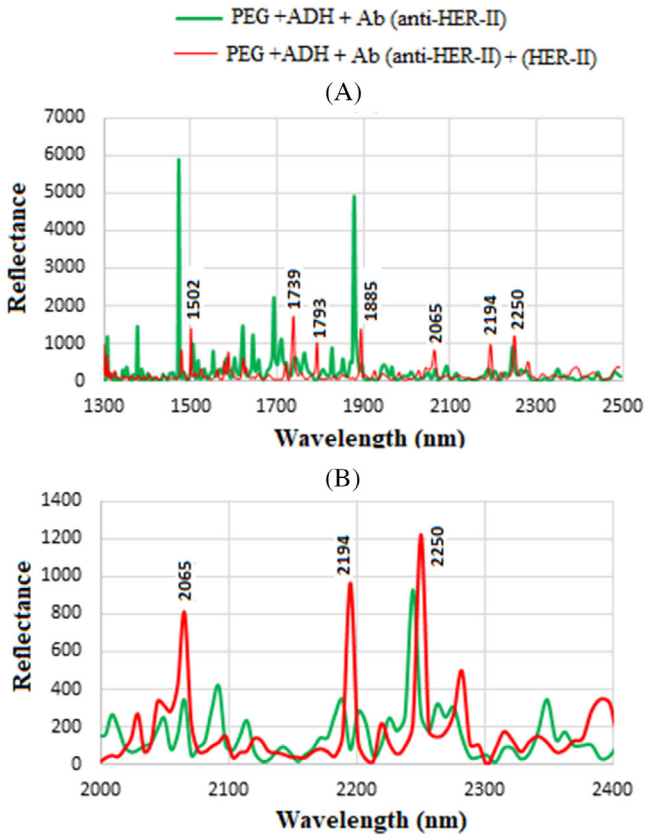

FIGURE 9 (A) Reflectance FT-NIR spectra of gold chip biosensor before and after interaction of functionalized gold surface with breast cancer blood serum. (B) Magnification of 2000 to 2400 nm region. FT-NIR, Fourier transform near-infrared

seen in Figure 8B which corresponds to the CH_2 aliphatic combination region. The signal in the aliphatic combination region is likely due to the presence of aliphatic amino acids such as glycine (Gly), alanine (Ala), valine (Val), leucine (Leu) and isoleucine (Ile) [63].

With the fabrication of the sensor chip complete, the next step was to observe the surface interaction with the analyte of interest (ie, antigen) which was the HER-II BC biomarker. Figure 9A shows a comparison of the FT-NIR spectra of the gold chip before and after interaction with the BCS sample as described in the methods. The signal at 1502 nm falls within the 1485 to 1515 nm region of the R—NH_2 1st overtone. The increase in signal is likely due to the increased presence of that group within the HER-II biomarker molecules since the —NH_2 group is a constituent of all amino acids. Another signal is seen at 1885 nm, which is in the R—COOH 1st overtone (O—H stretching) region. Once again, since the —COOH group is a constituent of amino acids, the signal is an indication of biomarker binding to the chip as the signal is considerably stronger compared to before HER-II binding as seen in Figure 9A. There is also a signal at 2065 nm, close to the 2055 nm

TABLE 2 SERS bands used for tentative band assignment of gold chip biomarker detection

Reference's band assignment	Wavenumber (cm^{-1})
Proteins	
Phenylalanine	622
Tyrosine	642; 640–650
Glycine, alanine v (C—N—C) assigned to the symmetric C—N—C stretch mode	850–900
Phenylalanine	1000–1010, 1103
Tyrosine	1166
Tryptophan	1220
β-sheet structure, amide III	1230–1240
Tryptophan, α helix	1300–1345
N—H primary and secondary amines and amides (stretch and bend)	1550–1640
C═O stretch (fairly broad)	1690–1710
C═O vibration	1720
—NH_3^+ I amine	2350–2750
O—H stretch (broad)	2400–3100
C—H antisym and sym stretching	2850–2990
═C—H stretch in aromatic and unsaturated hydrocarbons	3000–3100
NH_3^+ in amino acids	3000–3200
N—H primary and secondary amines and amides (stretch and bend)	3100–3500
—NH_2 in aromatic amines, primary amines and amides	3320–3520
—NH_2 in primary amides	3340–3360
Carbohydrates	
D(+) mannose	958, 1369
D(+) fucose	1256
Sialic acid	1002, 1237, 1391

Abbreviation: SERS, surface-enhanced Raman scattering.

β-sheet region, and two more signals at 2194 and 2250 nm that are in the R—NH_2 combination region and α-helix regions, respectively (Figure 9B). The collective analysis of these FT-NIR signals allows for confirmation of biomarker binding to the surface of the functionalized gold chip based on changes in the detected molecular signals.

3.3 | RS and SERS

SERS has been used to study protein binding orientation [57], characterize protein activity [64] and detect

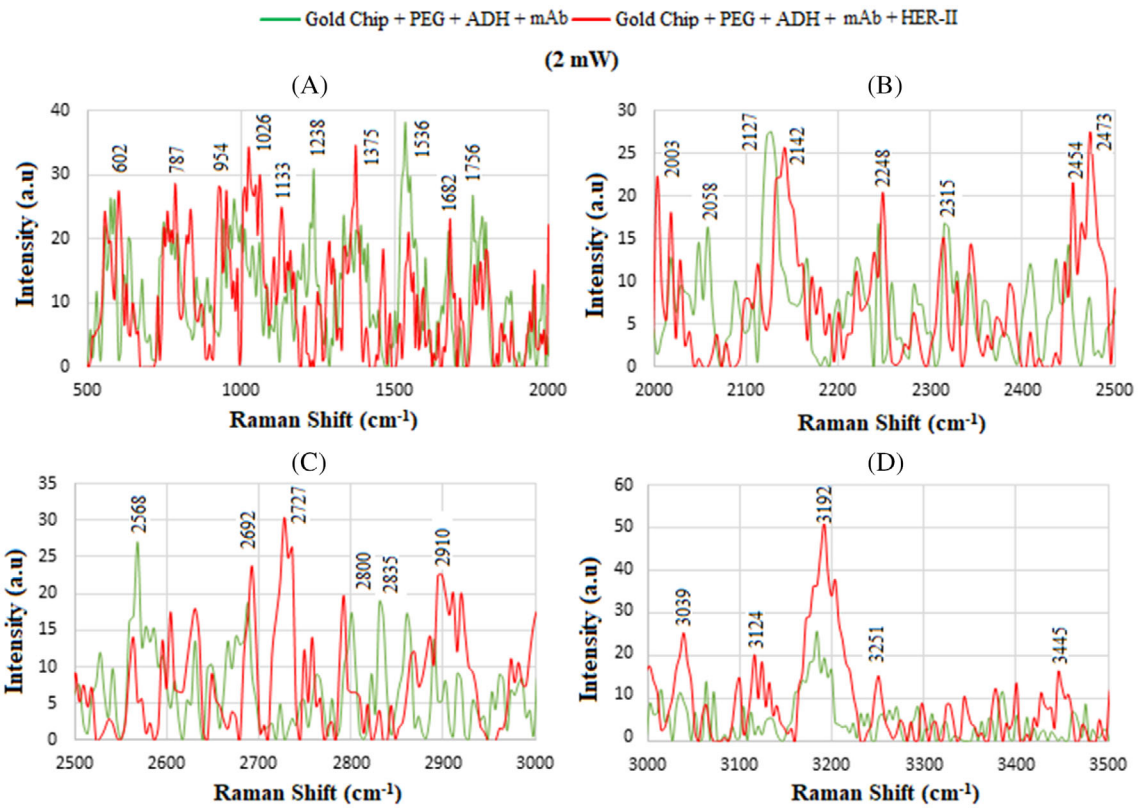

FIGURE 10 SERS spectra of the gold chip biosensor before and after biomarker binding at 637 nm and 2 mW laser power divided into (A) 500 to 2000 cm^{-1}, (B) 2000 to 2500 cm^{-1}, (C) 2500 to 3000 cm^{-1} and (D) 3000 to 3500 cm^{-1} regions. SERS, surface-enhanced Raman scattering

molecules based on their Raman fingerprint in biosensor applications [65]. In this work, although the gold chip surface is optically smooth, the nanoscale interparticle gaps between the deposited gold nanoparticles serve as a factor of enhancement for SERS [66]. As a complementary technique to FT-NIR spectroscopy, SERS was used to (a) investigate the surface chemistry of the gold chip biosensor during its fabrication and (b) confirm the BC biomarker binding to the functionalized surface of the biosensor. The spectral range of 500 to 3500 cm^{-1} is known to include signals for many protein components including individual amino acids such as Phe, Trp, Tyr and His, as well as disulfide bonds and secondary protein structures (ie, α-helices and β-sheets) and individual C—O, C—C, C—H and NH_3^+ bonds along with associated stretches and vibrational modes [67]. The general band assignments used for RS of proteins can be found in Table 2 [68–71]. The Raman signals from the biosensor are considered to be SERS signals as they are enhanced by the plasmonic confinement of the SPP by imperfections on the gold film surface [72]. This SERS activity arises from the uniform distribution of e-beam-deposited nanoparticles (grains) on the gold substrate.

For the analysis of the Raman shifts at 637 nm, the spectral average Raman shifts were calculated at each laser power (ie, 2, 4, 8 mW) using the average of three trials in Excel. Figure 10 shows the spectral average shifts at 2 mW laser power, divided into (A) 500 to 2000 cm^{-1}, (B) 2000 to 2500 cm^{-1}, (C) 2500 to 3000 cm^{-1} and (D) 3000 to 3500 cm^{-1} regions for ease of peak analysis. In Figure 10A, there are a number of peaks that increase after biomarker binding at 954, 1026 and 1375 cm^{-1} which are in the C—O stretch and C—C vibrational mode regions, respectively. In particular the mannose peak at 954 cm^{-1} is from the high mannose glycans of the HER-II biomarker [17, 70]. A second mannose peak can be seen at 1375 cm^{-1}. Interestingly, there is a decrease after biomarker binding at 1756 cm^{-1} in the C═O vibration region, which could indicate that the biomarker surface coverage is reducing the signal from the C═O bonds in the PEG linker molecules. In Figure 10B there is an increase in signal in the —NH_3^+ I amine and O—H stretch regions as seen by the peaks at 2454 and 2473 cm^{-1}, with another signal 2727 cm^{-1} (Figure 10C) in the same region. These regions are heavily influenced by the increased presence of biomarker proteins due to the abundance of —NH_3^+ groups and O—H bonds in amino acids. The strong signal

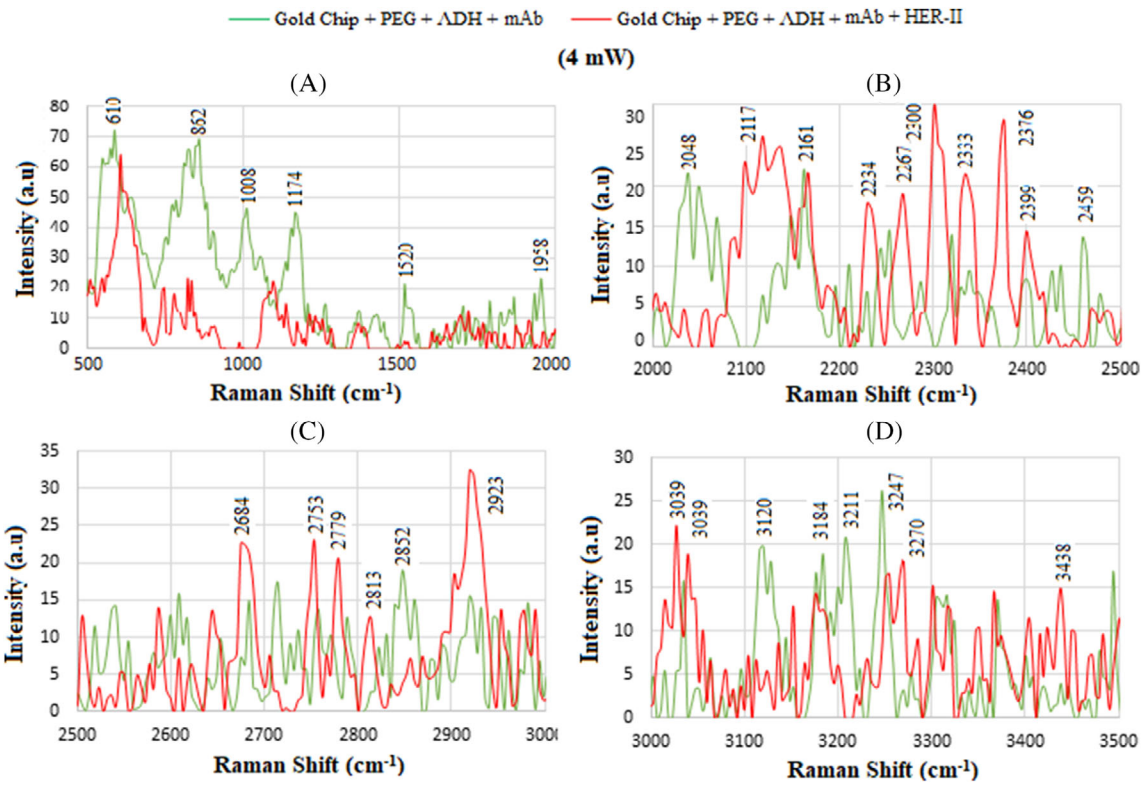

FIGURE 11 SERS spectra of the gold chip biosensor before and after biomarker binding at 637 nm and 4 mW laser power divided into (A) 500 to 2000 cm^{-1}, (B) 2000 to 2500 cm^{-1}, (C) 2500 to 3000 cm^{-1} and (D) 3000 to 3500 cm^{-1} regions. SERS, surface-enhanced Raman scattering

increase in Figure 10D at 3192 cm^{-1} is assigned to the NH_3^+ groups in amino acids as seen in Table 2. As expected, there is an increase in amino acid signal following biomarker binding to the gold chip.

Figure 11 shows the changes in Raman signal from the surface of the biosensor after the power was increased from 2 to 4 mW. Interestingly in Figure 11A, there is a decrease in signal following biomarker binding from several amino acids including Phe, Gly, Ala and Tyr at 610, 862, 1008 and 1174 cm^{-1}, respectively. It is expected that the signals increase with the increased protein presence of the biomarker molecules, however this was not observed. It is possible that the ratio of amino acids in the antibody and the biomarker resulted in a decreased signal since the composition of the antibody and biomarker are inherently unique. There may be a higher population of those specific amino acids in the mAb compared to the biomarkers themselves. In Figure 11B and C, the expected increase in NH_3^+ I amine and O—H stretch signals are seen at 2300, 2376, 2684 and 2753 cm^{-1}. In the 3000 to 3500 cm^{-1} regions, the peaks remain relatively constant as seen in Figure 11D, with no sharp increase in the NH_3^+ amino acid region as there was at 2 mW power. The peaks display nonlinear behavior in terms of intensity as it relates to power.

The power was increased from 4 to 8 mW to observe the changes in signal from the biosensor as presented in Figure 12. Similar to the results at 4 mW, in Figure 12A there is still a decrease in Phe, Gly and Ala signal with an increase in fucosylated glycans at 1250 cm^{-1}, sialic acid at 1400 cm^{-1} and in N—H amine/amide content at 1542 cm^{-1} relating to the glycosylated HER-II biomarker detected at the surface of the sensor. In Figure 12B there is an increase at 2400 cm^{-1} after biomarker binding which falls in the NH_3^+ I amine and O—H stretch region, indicating an increase in those bonds as they relate to proteins. The peaks in Figure 11C and D remain relatively constant before and after biomarker binding, again contributing to the observed nonlinear behavior of the peak intensity with increasing power.

The correlation between the metallic thin film and plasmonic device intrinsic characteristics can be studied via the optical absorption of metal interband and intraband electron transitions. For polycrystalline metal films, the electron scattering at surfaces and grain boundaries play a great role in losses [73] hence affecting the complex dielectric function [74]. The thickness of the metallic films varies from a few tens to hundreds of nanometers depending on the particular plasmonic application. Plasmonic materials are characterized by high real part

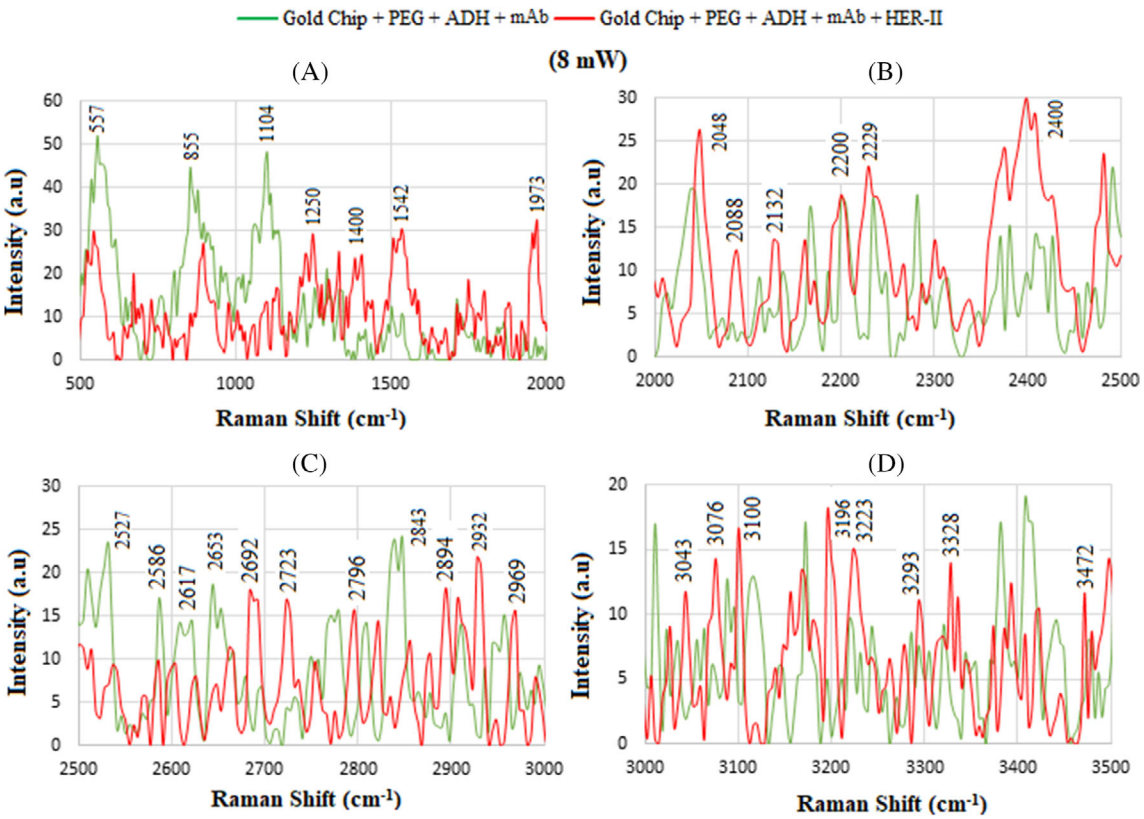

FIGURE 12 SERS spectra of the gold chip biosensor before and after biomarker binding at 637 nm and 8 mW laser power divided into (A) 500 to 2000 cm^{-1}, (B) 2000 to 2500 cm^{-1}, (C) 2500 to 3000 cm^{-1} and (D) 3000 to 3500 cm^{-1} regions. SERS, surface-enhanced Raman scattering

permittivity ε' and a low imaginary part ε'' responsible for losses, that is, $\varepsilon'' \ll |\varepsilon'|$. It has been suggested that for the film thickness less than 20 nm one can get island or highly roughened surfaces and quantum confinement effects should be considered while for a thickness of more than 200 nm, the film will behave as a bulk metal [75, 76]. To characterize the optical properties of Au thin films of various thicknesses, the Drude theory can describe the optical response of metals by

$$\varepsilon = \varepsilon'' + i\varepsilon'' = \varepsilon_\infty - \frac{\omega_p^2}{\omega^2 - i\gamma\omega}, \quad (2)$$

$$\varepsilon = \varepsilon_\infty - \frac{\omega_p^2}{\omega^2 + \gamma^2} + \frac{\gamma\omega_p^2}{\omega(\omega^2 + \gamma^2)}, \quad (3)$$

where ε_∞ is the infinite-frequency dielectric constant, ω_p is the plasma frequency of metal, the imaginary part of the dielectric function $\varepsilon'' = \gamma\omega_p^2/\omega(\omega^2 + \gamma^2)$ is responsible for the optical absorption in metal, $\gamma = \gamma_{ep} + \gamma_{eg} + \gamma_s$ is the damping factor of the Drude model, γ_{ep} is the total electron relaxation rate in bulk Au film due to electron-phonon scattering, γ_{eg} is the electron-grain boundary scattering and γ_s is the scattering on the surface of the metal film. According to Mayadas-Shatzkes (MS) theory [77, 78]

$$\gamma_{eg} = \gamma_{ep}\left\{\left[1 - \frac{3}{2}\alpha = 3\alpha^2 - 3\alpha^3 In\left(1 + \frac{1}{\alpha}\right)\right]^{-1} - 1\right\}, \quad (4)$$

where $\alpha = \frac{\Psi}{D}\left(\frac{R}{1-R}\right)$ and for Au bulk, $R = 4.6 \times 1013\,s^{-1}$ at room temperature is the grain-boundary reflection coefficient [79], and $\Psi = 39$ nm is the mean free path for electron conduction [80]. Therefore, as the average crystalline size D and the film thickness x decrease, both γ_{eg} and γ_s become stronger. In addition, it has been recently shown that the film thickness affects the optical properties and that below 80 nm, there is an underestimation of measured ε'' and γ [81–83].

3.4 | Analysis of variance (ANOVA) and peak distribution

With the use of a laser for RS, there is an inherent issue of laser-induced sample heating that comes with the

TABLE 3 Results of ANOVA test using three SERS peaks with a threshold intensity above 10 a.u. across three trials at each of 2, 4 and 8 mW laser powers

Source	Sum of squares (SS)	Degrees of freedom (df)	Mean squares (MS)	*F*-value	*p*-value	H_0 conclusion
Peak 590 cm^{-1}						
Between groups	994.659	2	497.330	1.456	0.305	Fail to reject
Within groups	2048.827	6	341.471			
Total	3043.486	8				
Peak 2205 cm^{-1}						
Between groups	357.852	2	178.926	0.964	0.433	Fail to reject
Within groups	1113.676	6	185.613			
Total	1471.528	8				
Peak 2919 cm^{-1}						
Between groups	5219.272	2	2609.636	3.706	0.090	Fail to reject
Within groups	4225.423	6	704.237			
Total	9444.695	8				

Abbreviations: ANOVA, analysis of variance; SERS, surface-enhanced Raman scattering.

application as previously reported in literature [84–86]. The extent of heating is highly dependent on the type of sample as well as the experimental conditions, and in this case, with a plasmonic metal thin film, the heating effects can be intensified. The SERS peak intensities are also known to depend on the orientation of the polarizability derivatives and the magnitude of the local field at the surface of the plasmonic metal surface [87]. Even in the case of smooth surfaces, the scattering of SP due to surface imperfections on the nanometer scale contributes to confinement of the resulting SPP and enhancement of the SERS signals [39]. In general, it was observed that the Raman shift intensities increased when the laser power was increased from 2 to 4 mW, but the intensities decreased when the power was further increased from 4 to 8 mW. This was likely due to laser-induced heating of the sample, as it has been suggested that strong laser sources may significantly decrease SERS signals due to desorption/degradation of the adsorbed molecules, annealing of the gold substrate and/or lateral particle diffusion induced by localized heating [88].

Given the nonlinearity of the intensity of Raman peaks at a given wavenumber with respect to laser power, an ANOVA test was implemented which considers the variance between groups (ie, 2, 4, and 8 mW laser power) and within groups (ie, three trials). The test was carried out to evaluate if increasing the laser power had an effect on peak intensity as hypothesized. To perform the analysis, the data was first sorted in Excel to determine which wavenumbers had intensities above a threshold value of 10 a.u. for all three trials in all three groups, selecting for a total of nine data points at a given wavenumber. These wavenumbers were determined to be 590, 2205 and 2919 cm^{-1}. The null hypothesis (H_0) was that there is no significant difference between the means of each group, meaning that changing the laser power (2, 4, 8 mW) does not affect the means of the Raman shifts at a given wavenumber between three trials. In order to reject the null hypothesis and prove that laser power does affect the intensities between 2, 4 and 8 mW, ANOVA has to return a *p*-value less than 0.05, suggesting that there is a less than 5% chance that any deviation from the null hypothesis is random. Table 3 shows a summary of the results from the ANOVA test at the three selected wavenumbers, which all failed to reject the null hypothesis. The *p*-values at 509, 2205 and 2919 cm^{-1} were calculated to be 0.305, 0.433 and 0.090, respectively, which collectively translates to a 9.0% to 43.3% probability that the variation in peak intensity with increasing power is random. The ANOVA test suggests that changing the laser power does not affect the peak intensity at a given Raman shift.

Additionally, the variation in the sum of the peak intensities was evaluated by taking the intensity sum for the entire spectrum for each of the three trials within a laser power, averaging them, and performing a second ANOVA test as summarized in Table 4. Here, H_0 was that there is no significant difference in the mean sum of the peak intensity between the three laser powers. It was

TABLE 4 Results of ANOVA test for average total SERS spectrum intensities across three trials at each of 2, 4 and 8 mW laser powers

Source	Sum of squares (SS)	Degrees of freedom (df)	Mean squares (MS)	*F*-value	*p*-value	H_0 conclusion
Between groups	21.668	2	10.834	2.486	0.164	Fail to reject
Within groups	26.147	6	4.358			
Total	47.815	8				

Abbreviations: ANOVA, analysis of variance; SERS, surface-enhanced Raman scattering.

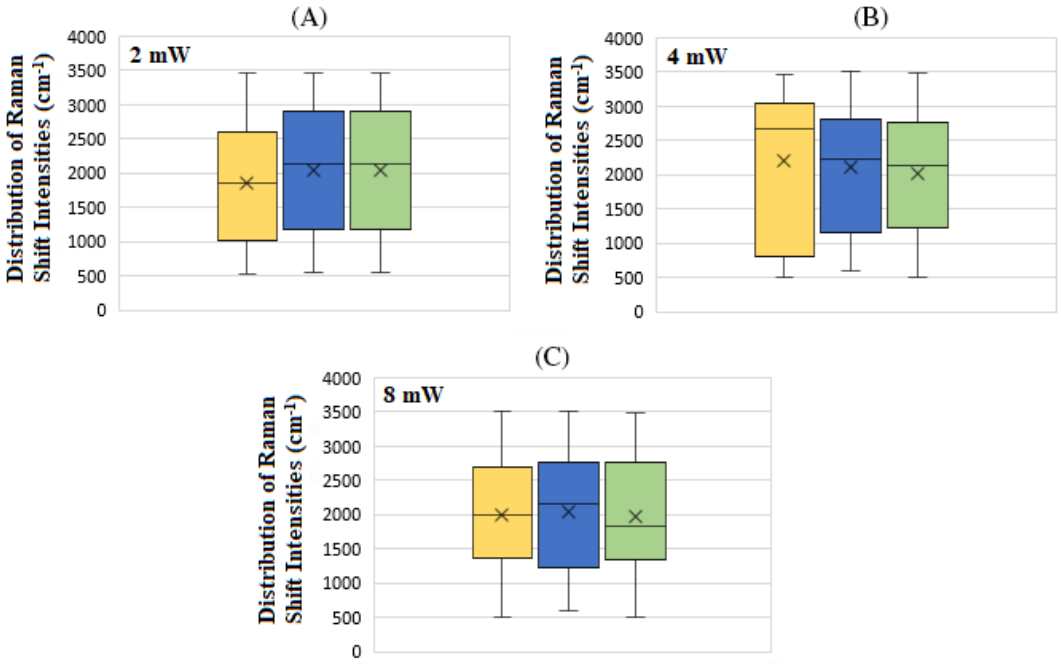

FIGURE 13 Box plot analysis of the distribution of Raman shift intensities above 10 a.u. after biomarker binding at (A) 2 mW, (B) 4 mW and (C) 8 mW laser powers

expected that the sum of peak intensity would increase as the laser power increased but again the data displayed nonlinear behavior, with a 16.4% probability that the variation of the average intensities between laser powers is random.

To better visualize the variance in peak distribution within the three trials as well as the three laser powers, a series of box plots were generated as seen in Figure 13 by plotting the wavenumbers that had a peak intensity above a 10 a.u. threshold. At 2 mW, the distributions are relatively constant between trials, with trial 1 showing a slight offset in distribution compared to trials 2 and 3 (Figure 13A). At 4 mW, the peak distribution shows more variation between trials, with a larger spread and median offset in trial 1 compared to the other trials (Figure 13B). At the final power of 8 mW, there is also variation, not so much in the spread of the distribution but more with the median of the data as it changes between trials (Figure 13C). Considering the ANOVA results and boxplot visualization, it is evident that the peak intensity exhibits nonlinear behavior as it relates to power. Although it is suggested that the changes in laser power do not have a significant effect on the variation in peak intensity, at the nanoscale, we believe the heating effects do play a role and continue to be a potential problem with RS approaches [84]. It is still within reason to propose that a power threshold was reached between 4 and 8 mW, which is why the shift intensities increased from 2 to 4 mW but decreased from 4 to 8 mW. This variance in SERS signal with power has been widely observed in literature with emphasis on the unpredictable gain/loss of SERS signals in heat-induced environments [88]. Similar SERS studies have also observed nonlinear SERS signals as a function of laser intensity and speculate that laser-induced heating effects can contribute to signal fluctuation [88, 89]. As mentioned above, the laser source can (a) cause degradation or photodamage of the sample

by photothermal heating effects [90, 91], (b) photothermally induce lateral diffusion of the biomolecules [92], (c) cause annealing of the biomolecules which can affect the signal from the area illuminated by the laser and (d) induce thermophoresis, that is, thermal diffusion or the Soret effect [93]. In the latter case, the heat from the laser produces a microscopic temperature gradient that can push analyte molecules out of the confined hot spots, effectively changing the molecular distribution within the heated area and corresponding SERS signals [93]. Together, these combined effects play a crucial role in laser-induced heating and result in variable SERS signals from both colloidal and substrate-based sensors.

4 | CONCLUSIONS

Characterization of the gold chip biosensor throughout the fabrication process by FT-NIR provided useful information on the surface chemistries involved, specifically regarding the proposed selective orientation EDC/ADH antibody conjugation method that has not been thoroughly investigated in literature. The presence of biomarker in the serum was evaluated with both FT-NIR and SERS methods, where the distinct BCS peaks showed promising results in terms of glycosylated protein detection. The nonlinearity of the SERS peak intensity with increasing power was assessed using ANOVA, which suggests that the laser power did not have a significant effect on the variation in peak intensity. However, at the nanoscale, the laser-induced heating effects should not be ignored as it a known factor for fluctuation of SERS signals, posing a challenge for the reproducibility of SERS data in this field. Further studies involving assessment of substrate temperature with increasing power would be of interest to investigate possible photothermal heating effects and thermophoresis. The results of this study are insightful in nanobiosensor development as it relates to sensor chip fabrication using oriented mAb, spectroscopic evaluation of biomarker binding, and observation of laser-induced heating effects on SERS signals.

ACKNOWLEDGMENTS

The authors would like to thank M.I.S. Electronics Inc. for supporting this research at the Nanobiophotonics & Biomedical Research Laboratory. We also thank York University for the use of AFM service.

CONFLICT OF INTEREST

The authors declare that they have no known competing financial interests or personal relationships that could have appeared to influence the work reported in this paper.

DATA AVAILABILITY STATEMENT

The data that support the findings of this study are available from the corresponding author upon reasonable request.

ETHICS STATEMENT

This research does not contain any form of studies with human participants or animals performed by any of the authors.

ORCID

Mohammad E. Khosroshahi https://orcid.org/0000-0002-6628-5569

REFERENCES

[1] R. Siegel, J. Ma, Z. Zou, A. Jemal, *CA Cancer J. Clin.* **2014**, *64*, 9.
[2] L. Fan, K. Strasser-Weippl, J. Li, J. St Louis, D. M. Finkelstein, K. Yu, W. Chen, Z. Shao, P. E. Goss, *Lancet Oncol.* **2014**, *15*, 27.
[3] S. Y. Loke, A. S. G. Lee, *Eur. J. Cancer* **2018**, *92*, 54.
[4] A. Kazarian, O. Blyuss, G. Metodieva, A. Gentry-Maharaj, A. Ryan, E. M. Kiseleva, O. M. Prytomanova, I. J. Jacobs, M. Widschwendter, U. Menon, J. F. Timms, *Br. J. Cancer* **2017**, *116*, 501.
[5] B. Handy, *Lab. Med.* **2009**, *40*, 99.
[6] H. Li, J. He, S. Li, A. P. F. Turner, *Biosens. Bioelectron.* **2013**, *43*, 25.
[7] Y. Liu, X. Weng, K. Wang, Y. Xue, A. Wang, L. Wu, J. Feng, *Sens. Actuators B Chem.* **2017**, *247*, 349.
[8] A. Khoshroo, M. Mazloum-Ardakani, M. Forat-Yazdi, *Sens. Actuators B Chem.* **2018**, *255*, 580.
[9] X. Jiang, H. Wang, R. Yuan, Y. Chai, *Biosens. Bioelectron.* **2015**, *63*, 33.
[10] Y. M. Park, S. J. Kim, K. Kim, Y. D. Han, S. S. Yang, H. C. Yoon, *Sens. Actuators B Chem.* **2013**, *186*, 571.
[11] X. Wang, H. Yu, D. Lu, J. Zhang, W. Deng, *Sens. Actuators B Chem.* **2014**, *195*, 630.
[12] A. W. Wang, R. Kiwan, R. M. White, R. L. Ceriani, *Sens. Actuators B Chem.* **1998**, *49*, 13.
[13] H. Zhu, P. S. Dale, C. W. Caldwell, X. Fan, *Anal. Chem.* **2009**, *81*, 9858.
[14] S. A. Albagoush, F. Limaiem, *StatPearls [Internet]*, StatPearls Publishing LLC, Treasure Island, FL **2022**, p. NBK537134.
[15] A. Shamshirian, A. R. Aref, G. W. Yip, M. Ebrahimi Warkiani, K. Heydari, S. Razavi Bazaz, Z. Hamzehgardeshi, D. Shamshirian, M. Moosazadeh, R. Alizadeh-Navaei, *BMC Cancer* **2020**, *20*, 1049.
[16] D. A. Scott, R. R. Drake, *Expert Rev. Proteomics* **2019**, *16*, 665.
[17] K. Ščupáková, O. T. Adelaja, B. Balluff, V. Ayyappan, C. M. Tressler, N. M. Jenkinson, B. S. R. Claes, A. P. Bowman, A. Cimino-Mathews, M. J. White, P. Argani, R. M. A. Heeren, K. Glunde, *JCI Insight* **2021**, *6*, 146945.
[18] D. Cialla-May, M. Schmitt, J. Popp, *Phys. Sci. Rev.* **2019**, *4*, 20170040.
[19] N. Stone, M. C. Hart Prieto, P. Crow, J. Uff, A. W. Ritchie, *Anal. Bioanal. Chem.* **2007**, *387*, 1657.

[20] L. Silveira, K. R. M. Leite, F. L. Silveira, M. Srougi, M. T. T. Pacheco, R. A. Zângaro, C. A. Pasqualucci, *Laser Med. Sci.* **2014**, *29*, 1469.
[21] K. Eberhardt, C. Stiebing, C. Matthäus, M. Schmitt, J. Popp, *Expert Rev. Mol. Diagn.* **2015**, *15*, 773.
[22] J. Homola, *Chem. Rev.* **2008**, *108*, 462.
[23] M. Kahraman, E. R. Mullen, A. Korkmaz, S. Wachsmann-Hogiu, *Nano* **2017**, *6*, 831.
[24] R. A. Álvarez-Puebla, *J. Phys. Chem. Lett.* **2012**, *3*, 857.
[25] G. P. Szekeres, J. Kneipp, *Front. Chem.* **2019**, *7*, 7.
[26] F. Shan, X. Zhang, X. Fu, L. Zhang, D. Su, S. Wang, J. Wu, T. Zhang, *Sci. Rep.* **2017**, *7*, 6813.
[27] S. He, J. Chua, E. K. M. Tan, J. C. Y. Kah, *RSC Adv.* **2017**, *7*, 16264.
[28] R. Tantra, R. J. C. Brown, M. J. T. Milton, *J. Raman Spectrosc.* **2007**, *38*, 1469.
[29] K. Hanna, E. Krzoska, A. M. Shaaban, D. Muirhead, R. Abu-Eid, V. Speirs, *Br. J. Cancer* **2022**, *126*, 1125.
[30] R. F. Aroca, R. A. Alvarez-Puebla, N. Pieczonka, S. Sanchez-Cortez, J. V. Garcia-Ramos, *Adv. Colloid Interf. Sci.* **2005**, *116*, 45.
[31] Z. Wang, Z. Zhang, in *Advanced Nano Deposition Methods* (Eds: Y. Lin, X. Chen), Wiley-VCH Verlag GmbH, Weinheim **2016**, p. 33.
[32] Y. Wang, E. Wang, in *Surface Enhanced Raman Spectroscopy: Analytical, Biophysical and Life Science Applications* (Ed: S. Schlücker), Wiley-VCH Verlag GmbH & Co, KGaA, Weinheim **2011**, p. 39.
[33] D. Erickson, S. Mandal, A. H. Yang, B. Cordovez, *Microfluid. Nanofluid.* **2008**, *4*, 33.
[34] D. Dey, T. Goswami, *J. Biomed. Biotechnol.* **2011**, *2011*, 348218.
[35] T. Lee, T. Kim, J. Yoon, Y. Chung, J. Y. Lee, J. Choi, *Sensors* **2016**, *16*, 660.
[36] B. Khlebtsov, V. Zharov, A. Melnikov, V. Tuchin, N. Khlebtsov, *Nanotechnology* **2006**, *17*, 5167.
[37] X. Huang, P. K. Jain, I. El-Sayed, M. El-Sayed, *Nanomedicine* **2007**, *2*, 681.
[38] C. Urban, A. S. Urban, H. Charron, A. Joshi, *Transl. Cancer Res.* **2013**, *2*, 292.
[39] R. Malureanu, A. Lavrinenko, *Nanotechnol. Rev.* **2015**, *4*, 259.
[40] F. C. Breedveld, *Lancet* **2000**, *355*, 735.
[41] J. M. Reichert, C. J. Rosensweig, L. B. Faden, M. C. Dewitz, *Nat. Biotechnol.* **2005**, *23*, 1073.
[42] G. Jalani, M. Cerruti, *Nanoscale* **2015**, *7*, 9990.
[43] C. Pasquini, *Anal. Chim. Acta* **2018**, *1026*, 8.
[44] Y. Ozaki, Y. Morisawa, in *Near-Infrared Spectroscopy* (Eds: Y. Ozaki, C. Huck, S. Tsuchikawa, S. B. Engelsen), Springer, Singapore **2021**, p. 11.
[45] K. B. Beć, C. W. Huck, *Front. Chem.* **2019**, *7*, 48.
[46] M. R. Kierny, T. D. Cunningham, B. K. Kay, *Nanotechnol. Rev.* **2012**, *3*, 17240.
[47] S. Kumar, J. Aaron, K. Sokolov, *Nat. Protoc.* **2008**, *3*, 314.
[48] C. J. Alan, in *Spectroscopy of Surfaces (Advances in Spectroscopy)* (Eds: R. J. H. Clark, R. E. Hester), Wiley, New York **1988**, p. 37.
[49] M. Pereira, E. P. C. Lai, *J. Nanobiotechol.* **2008**, *6*, 10.
[50] P. J. Conroy, S. Hearty, P. Leonard, R. J. O'Kennedy, *Semin. Cell Dev. Biol.* **2009**, *20*, 10.
[51] E. J. Blackie, E. C. Le Ru, P. G. Etchegoin, *J. Am. Chem. Soc.* **2009**, *131*, 14466.
[52] K. A. Willets, R. P. Van Duyne, *Annu. Rev. Phys. Chem.* **2007**, *58*, 267.
[53] C. Hsieh, Y. Huang, M. Sheu, H. Ho, *Int. J. Biol. Macromol.* **2014**, *64*, 45.
[54] E. M. A. Mohamed, W. H. Eisa, T. Abdel-Baset, S. Mahrous, *Int. J. Adv. Sci. Res.* **2017**, *3*, 65.
[55] J. Herzberger, K. Niederer, H. Pohlit, J. Seiwert, M. Worm, F. R. Wurm, H. Frey, *Chem. Rev.* **2016**, *116*, 2170.
[56] L. H. Fornander, B. Feng, T. Beke-Somfai, B. Nordén, *J. Phys. Chem. B* **2014**, *118*, 9247.
[57] I. H. M. van Stokkum, H. Linsdell, J. M. Hadden, P. I. Haris, D. Chapman, M. Bloemendal, *Biochemistry* **1995**, *34*, 10508.
[58] B. Stuart, *Infrared Spectroscopy: Fundamentals and Applications*, John Wiley & Sons Ltd, West Sussex **2004**, p. 137.
[59] M. Ishigaki, Y. Ozaki, in *Vibrational Spectroscopy in Protein Research* (Eds: Y. Ozaki, M. Baranska, I. Lednev, B. R. Wood), Elsevier, London (UK) **2020**, p. 144.
[60] A. B. Eldin, in *Wide Spectra of Quality Control* (Ed: I. Akyar), InTech Open, London (UK) **2011**, p. 237.
[61] K. Izutsu, Y. Fujimaki, A. Kuwabara, Y. Hiyama, C. Yomota, N. Aoyagi, *J. Pharm. Sci.* **2006**, *95*, 781.
[62] G. A. Sprenger, in *Amino Acid Biosynthesis: Pathways, Regulation and Metabolic Engineering* (Ed: V. F. Wendisch), Springer, Berlin **2007**, p. 93.
[63] A. Ganesan, M. J. Brunger, F. Wang, *Eur. Phys. J. D* **2013**, *67*, 229.
[64] N. Feliu, M. Hassan, E. Garcia Rico, D. Cui, W. Parak, R. Alvarez-Puebla, *Langmuir* **2017**, *33*, 9711.
[65] I. Bruzas, W. Lum, Z. Gorunmez, L. Sagle, *Analyst* **2018**, *143*, 3990.
[66] N. U. Ahamad, M. Al-Amin, A. Ianoul, *J. Nanopart.* **2014**, *2014*, 602385.
[67] N. Kuhar, S. Sil, S. Umapathy, *Spectrochim. Acta A Mol. Biomol. Spectrosc.* **2021**, *258*, 119712.
[68] E. Vargas-Obieta, J. C. Martínez-Espinosa, B. E. Martínez-Zerega, L. F. Jave-Suárez, A. Aguilar-Lemarroy, J. L. González-Solís, *Laser Med. Sci.* **2016**, *31*, 1317.
[69] A. Ortiz-Dosal, E. Loredo-García, A. G. Álvarez-Contreras, J. M. Núñez-Leyva, L. Ortiz-Dosal, E. Kolosovas-Machuca, *J. Nanomater.* **2021**, *2021*, 8874193.
[70] K. De Gussem, PhD Thesis, Ghent University (Belgium), **2008**.
[71] A. Hernández-Arteaga, D. J. Z. Nava, E. K.-M. José, J. J. Velázquez-Salazar, E. Vinogradova, M. José-Yacamán, H. Navarro-Contreras, *Nano Res.* **2017**, *10*, 3662.
[72] M. Bauch, K. Toma, M. Toma, Q. Zhang, J. Dostalek, *Plasmonics* **2014**, *9*, 781.
[73] A. F. Mayadas, M. Shatzkes, *Phys. Rev. B* **1970**, *1*, 1382.
[74] J. Sotelo, J. Ederth, G. Niklasson, *Phys. Rev. B* **2003**, *67*, 195106.
[75] H. Qian, Y. Xiao, D. Lepage, L. Chen, Z. Liu, *Nano* **2015**, *4*, 413.
[76] X. D. Li, T. P. Chen, Y. Liu, K. C. Leong, *J. Nanopart. Res.* **2015**, *17*, 67.
[77] A. F. Mayadas, M. Shatzkes, J. Janak, *Appl. Phys. Lett.* **1969**, *14*, 345.
[78] D. Y. Fedyanin, A. V. Krasavin, A. V. Arsenin, A. V. Zayatus, *Nano Lett.* **2012**, *12*, 2459.
[79] G. R. Parkins, W. E. Lawrence, R. W. Christy, *Phys. Rev. B* **1981**, *23*, 6408.

[80] E. H. Sondheimer, *Adv. Phys.* **1952**, *1*, 1.
[81] K. M. McPeak, S. Jayanti, S. Kress, S. Meyer, S. Iotti, A. Rossinelli, D. J. Norris, *ACS Photonics* **2015**, *2*, 326.
[82] J. H. Park, P. Ambwani, M. Manno, N. C. Lindquist, P. Nagpal, S. Oh, C. Leighton, D. Norris, *Adv. Mater.* **2012**, *24*, 3988.
[83] D. I. Yakubovsky, A. V. Arsenin, Y. V. Stebunov, D. Y. Fedyanin, V. Volkov, *Opt. Express* **2017**, *25*, 25574.
[84] J. Johansson, S. Pettersson, L. S. Taylor, *J. Pharm. Biomed. Anal.* **2002**, *30*, 1223.
[85] K. Morishita, M. Nara, S. Amari, J. Matsuda, *Spectrosc. Lett.* **2011**, *44*, 459.
[86] N. J. Everall, J. Lumsdon, D. J. Christopher, *Carbon* **1991**, *29*, 133.
[87] Y. Wang, E. Wang, in *Surface Enhanced Raman Spectroscopy: Analytical, Biophysical and Life Science Applications* (Ed: S. Schlücker), Wiley-VCH Verlag GmbH, Weinheim **2015**, p. 39.
[88] J. H. Kim, K. M. Twaddle, L. M. Cermak, W. Jang, J. Yun, H. Byun, *Colloid Surf. A* **2016**, *498*, 20.
[89] J. Langer, D. Jimenez de Aberasturi, J. Aizpurua, R. A. Álvarez-Puebla, B. Auguié, J. J. Baumberg, G. C. Bazan, S. E. J. Bell, A. Boisen, A. G. Brolo, J. Choo, D. Cialla-May, V. Deckert, L. Fabris, K. Faulds, F. J. G. de Abajo, R. Goodacre, D. Graham, A. J. Haes, C. L. Haynes, C. Huck, T. Itoh, M. Kall, J. Kneipp, N. A. Kotov, H. Kuang, E. C. Le Ru, H. K. Lee, J. Li, X. Y. Ling, S. A. Maier, T. Mayerhöfer, M. Moskovits, K. Murakoshi, J. Nam, S. Nie, Y. Ozaki, I. Pastoriza-Santos, J. Perez-Juste, J. Popp, A. Pucci, S. Reich, B. Ren, G. C. Schatz, T. Shegai, S. Schlücker, L. Tay, K. G. Thomas, Z. Tian, R. P. Van Duyne, T. Vo-Dinh, Y. Wang, K. A. Willets, C. Xu, H. Xu, Y. Xu, Y. S. Yamamoto, B. Zhao, L. M. Liz-Marzan, *ACS Nano* **2020**, *14*, 28.
[90] M. A. De Jesúsm, K. S. Giesfeldt, M. J. Sepaniak, *Appl. Spectrosc.* **2003**, *57*, 429.
[91] Y. Fang, N. Seong, D. D. Dlott, *Science* **2008**, *321*, 388.
[92] K. W. Kho, Z. X. Shen, Z. Lei, F. Watt, K. C. Soo, M. Olivo, *Anal. Chem.* **2007**, *79*, 8870.
[93] T. Kang, S. Hong, Y. Choi, L. P. Lee, *Small* **2010**, *6*, 2649.

How to cite this article: M. E. Khosroshahi, Y. Patel, *J. Biophotonics* **2022**, e202200252. https://doi.org/10.1002/jbio.202200252